

Research paper

Research on passive adaptive wall-climbing cleaning and inspection robot of marine cylindrical steel structure based on conical magnetic adsorption wheel



Gaosheng Luo ^a, Chuankun Luo ^a, Shimin Gao ^a, Jingxiang Xu ^a, Xuteng Bao ^{a,b}, Zhiqiang Ma ^a,
Zhe Jiang ^{a,c,*}

^a Shanghai Engineering Research Center of Hadal Science and Technology, College of Engineering Science and Technology, Shanghai Ocean University, Shanghai, 201306, China

^b Fishery Machinery and Instrument Research Institute, Chinese Academy of Fishery Science, Shanghai, 200092, China

^c Lanqi Robot Co., Ltd, Wuxi, Jiangsu, 214122, China

ARTICLE INFO

Keywords:

Wall-climbing cleaning and inspection robot
Cylindrical steel structure
Passive adaptive
Conical magnetic adsorption wheelsets
Prototype experiments

ABSTRACT

The marine growth cleaning and structural defect detection of steel structures of offshore underwater facilities are essential parts of the inspection and maintenance of offshore platforms. However, a majority part of underwater structures of offshore facilities, such as offshore wind turbines, Jacket platforms, Jack-up platforms, etc., are cylindrical structures. Compared with the planar structures, cylindrical structures have large curvature, and less supporting area, and therefore put forward higher requirements for the performance of the attached surface working robot. This paper proposes a wall-climbing cleaning robot that can move freely on the wall of cylindrical steel structures and passively adapt to cylindrical structures with various curvatures and diameters. According to the structural characteristics of the robot, a static failure model is established to analyze the different instability forms of the robot and the minimum critical magnetic adsorption force is determined. To ensure the minimum mass and the maximum magnetic adsorption force of the conical magnetic adsorption wheelsets, the effects of air gap and cone angle on the performance of the conical magnetic adsorption wheelsets were analyzed parametrically, and the optimal structural size was obtained. Finally, the mobility and capability of the robot on the surface of the different diameter cylindrical structures has been validated through prototype experiments.

1. Introduction

The offshore jacket platform is a pile foundation platform widely used in soft soil foundations. In addition to being eroded by seawater, its underwater structure can quickly become a habitat for marine organisms' growth and reproduction. The habitat and reproduction of these aquatic organisms not only cause biological corrosion to the jacket column but also change the mechanical properties, weaken the load capacity (Jimenez-Martinez, 2020), shorten the life of the jacket platform, causing serious safety hazards (Albitar et al., 2014; Hachicha et al., 2019). Therefore, it is essential to clean up the growth and corrosion products on the jacket column in time (Callow and Callow, 2002). Currently, the cleaning and detection of the offshore jacket

platform are still carried out manually. Still, some problems exist, such as high labor intensity, long construction periods, poor safety, and low cleaning efficiency (Poggi et al., 2020).

In recent years, wall-climbing robots have developed rapidly, and according to their adsorption methods, they can be divided into vacuum (negative pressure) adsorption, magnetic adsorption, and bionic adsorption (Chang, 2015; Wei et al., 2018; Zhang et al., 2021). The offshore jacket platform is primarily a TKY-type connection structure. The TKY-type tubular joint, with a complex three-dimensional surface, is the most critical and common connection form in space steel structures (Lu et al., 2013). Due to the complexity of sea conditions and the complexity of the platform jacket structure, the magnetic adsorption technology is commonly adopted to improve the reliability of

* Corresponding author. Shanghai Engineering Research Center of Hadal Science and Technology, College of Engineering Science and Technology, Shanghai Ocean University, Shanghai 201306, China.

E-mail address: zjiang@shou.edu.cn (Z. Jiang).

Table 1

Notable climbing inspection robots.

Robot	Locomotion Type	Specification	Climbing Capability	Adhesion
[Huang et al., 2017]	 Roller-chains	300 × 200 × 84 mm 10 kg 0.12 m/s	Flat ✓ Concave ✗ Convex ✗ Cylinder ✗ Edge transition ✗	Permanent Magnet (Touched) ^a
[Huang et al., 2017]	 4 differential wheels drive	150 × 221 × 241 mm 6 kg	Flat ✓ Concave ✗ Convex ✗ Cylinder ✓ Edge transition ✓	Permanent Magnet (Touched) ^a
[Nguyen and La, 2019]	 2 motorized roller-chains and 1 motorized transformation	163 × 145 × 198 mm 3 kg 0.35 m/s	Flat ✓ Concave ✓ Convex ✓ Cylinder ✓ Edge transition ✓	Permanent Magnet (Touched) ^a
[Nguyen et al., 2020]	 Hybrid mobile-worming configuration	700 × 500 × 300 mm 12 kg 0.2 m/s	Flat ✓ Concave ✓ Convex ✓ Cylinder ✓ Edge transition ✓	Permanent Magnet (Untouched) ^b
[Pham et al., 2021]	 Drone mode and 4 differential wheels drive	/	Flat ✓ Concave ✗ Convex ✗ Cylinder ✓ Edge transition ✗	Permanent Magnet (Touched) ^a
[Pham et al., 2022]	 4 differential wheels drive	457 × 312 × 217 mm 12 kg	Flat ✓ Concave ✗ Convex ✗ Cylinder ✓ Edge transition ✓	Permanent Magnet (Touched) ^a
[Nguyen et al., 2023]	 Bicycle-like and multisteering movement	150 × 80 × 90 mm 2 kg 0.2 m/s	Flat ✓ Concave ✓ Convex ✓ Cylinder ✓ Edge transition ✓	Permanent Magnet (Touched) ^a

^a The permanent magnet is in direct contact with the adsorption surface.^b The distance between the permanent magnet and the adsorption surface is 1 mm.

operations. Traditional wall-climbing robots are designed with permanent magnet wheels or permanent magnet tracks (Huang et al., 2017). However, they either cannot adapt to various cylindrical structures of different curvatures due to their structural characteristics or sacrifice their load capacity to increase their moving flexibility, which affects their efficiency (Le et al., 2020; Han et al., 2021).

To increase the motion performance of the robot on the cylindrical

structure's surface while ensuring efficiency, some researchers have designed and developed unique magnetic adsorption wall-climbing robots. As shown in Table 1, Nguyen and La (2019; 2021) proposed a tracked magnetic adsorption wall-climbing robot with reciprocating mechanism. It can change its posture and adapt to different surfaces (such as flat, convex, concave, and cylindrical) (Yang et al., 2024). However, embedding permanent magnets directly into polyurethane is

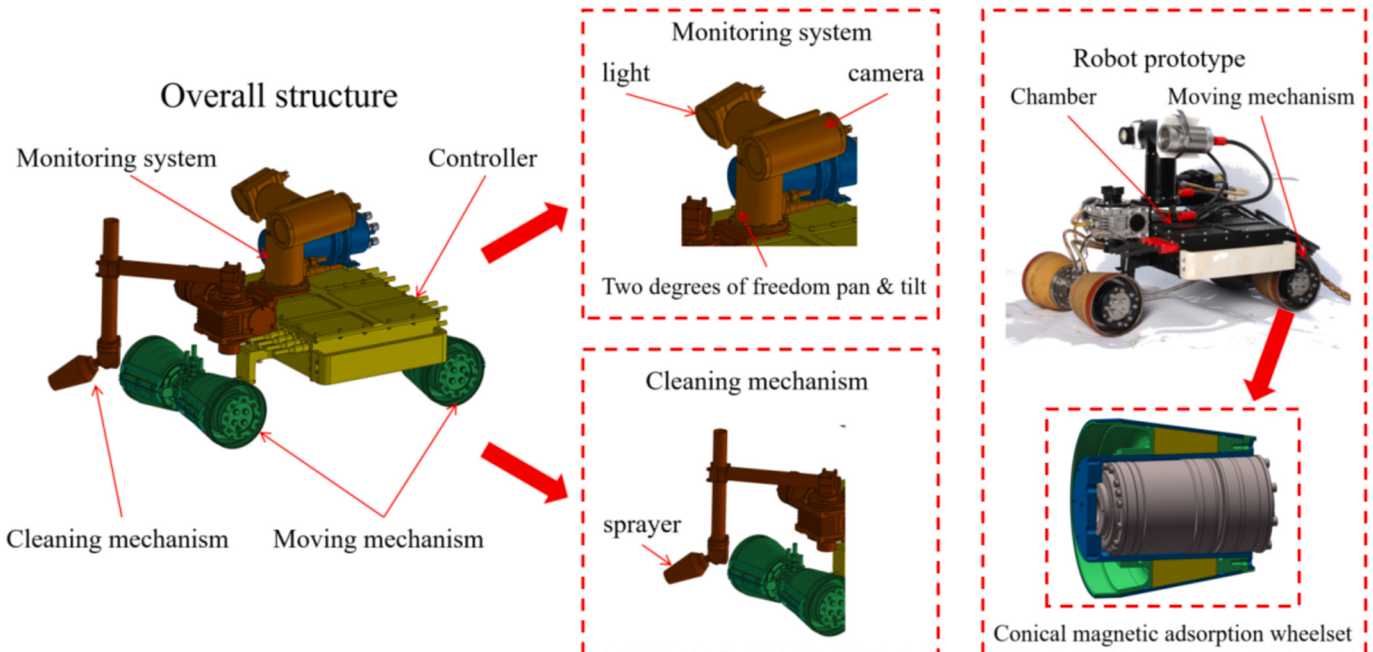


Fig. 1. The overall structure of the wall-climbing cleaning robot and its magnetic adsorption wheelsets for offshore cylindrical steel structures.

likely to cause corrosion and damage to permanent magnets, and the high overall center of gravity of the robot due to the reciprocating mechanism affects the adsorption performance (La H et al., 2019; Yang et al., 2021). Wang et al. (2022) proposed a flexible wheel-legged composite motion mechanism that can change its rigidity to complete the transition of the wall (Nguyen et al., 2020). Espinoza et al. (2015) proposed a wheeled magnetic adsorption robot. The left and right magnetic wheels are arranged in dislocation, and the electromagnet is placed in the robot's abdomen, which improves the motion performance of the robot in the cylindrical structure.

The magnetic adsorption wheeled mobile robot proposed by Leon-Rodriguez et al. (2012) adopts a three-stage design, which can adapt to different surface curvatures and achieve a 90° wall span. Silva et al. (2013) proposed a magnetic adsorption wheeled robot, which can provide sufficient magnetic adsorption force by actively adjusting the magnetic adsorption force. Li and Wang, 2016 proposed an omnidirectional mobile robot equipped with Mecanum wheels, and its adsorption device was installed on the wheel (Tavakoli et al., 2012). They can change the position and magnetic force of the magnet in three degrees of freedom to adapt to the different curvature of the tank wall.

Although the above machines can move on various walls (such as planes, convex surfaces, concave surfaces, curved surfaces, cylindrical surfaces, etc.), the prototype experiment only does forward movement, and its turning motion performance on the surface of the cylindrical structure is not precise. The whole machine integration and sealing is not high, can only be used in a dry environment, and is unsuitable for underwater cleaning operations. Given the above problems, this paper proposes a passive adaptive conical wheel magnetic adsorption wall-climbing cleaning robot for offshore cylindrical steel structures, which is composed of two degrees of freedom passive adaptive structural components and an embedded conical magnetic adsorption wheel so that the four magnetic wheels of the robot can always contact the cylindrical structures with different curvatures, which ensures that the robot moves stably and freely on the surfaces of the cylindrical structures.

This paper is organized as follows: In section 2, the overall structure of the robot is summarized, and the adaptive structure of the robot and the design of the conical magnetic adsorption wheelset are introduced in detail. In section 3, stability analysis is carried out to determine the

minimum magnetic adsorption force required by the robot for cleaning operations. In section 4, the detailed design of the magnetic adsorption module is carried out, the magnetic circuit is determined, and the optimal structural parameters are obtained. In section 5, the structural parameters of the conical magnetic adsorption wheelset are analyzed and optimized, and the experiments and discussions are carried out in section 6. The epilogue is the end of the text.

2. The overall structure design of the wall-climbing robot

The overall structure of the magnetic adsorption wall-climbing cleaning robot proposed in this paper is shown in Fig. 1. The size of the robot is 782 × 495 × 326 mm (Length × Width × Height), and the dry weight is about 52 kg. The robot has two sets of conical magnetic adsorption wheels in the front and back to realize the adsorption and movement on the wall of the large curvature outer circular steel structure. An ultra-high pressure water jet nozzle assembly is equipped on the top and connected to the ultra-high pressure water pump on the offshore jacket platform through the ultra-high pressure water pipe. A two-degree-of-freedom pan and tilt equipped with a camera and a compensation lamp is mounted on the top to create a monitoring system.

In addition to the above design, the structural characteristics of the cylindrical structure should also be fully considered. Firstly, the wall-climbing robot should be able to move freely along the cylindrical structure of the offshore jacket platform and have good steering performance and movement flexibility. Secondly, it should also be able to cross obstacles such as welds and raised structures. Finally, the robot should be compact in structure and have significant magnetic adsorption-force-to-mass ratio. This paper adopts a four-wheel independent drive, and a novel passive adaptive structure is proposed to improve the robot's maneuverability. It can adapt to the variable curvature structure with different diameters.

2.1. Passive adaptive structure

For the current wheeled robot, when it moves helically or turns in place on a cylindrical structure, its four wheels cannot always be in contact with the wall at the same time, and there is a risk of the robot falling (Guang-Ming et al., 2003). To ensure that each wheel is in contact

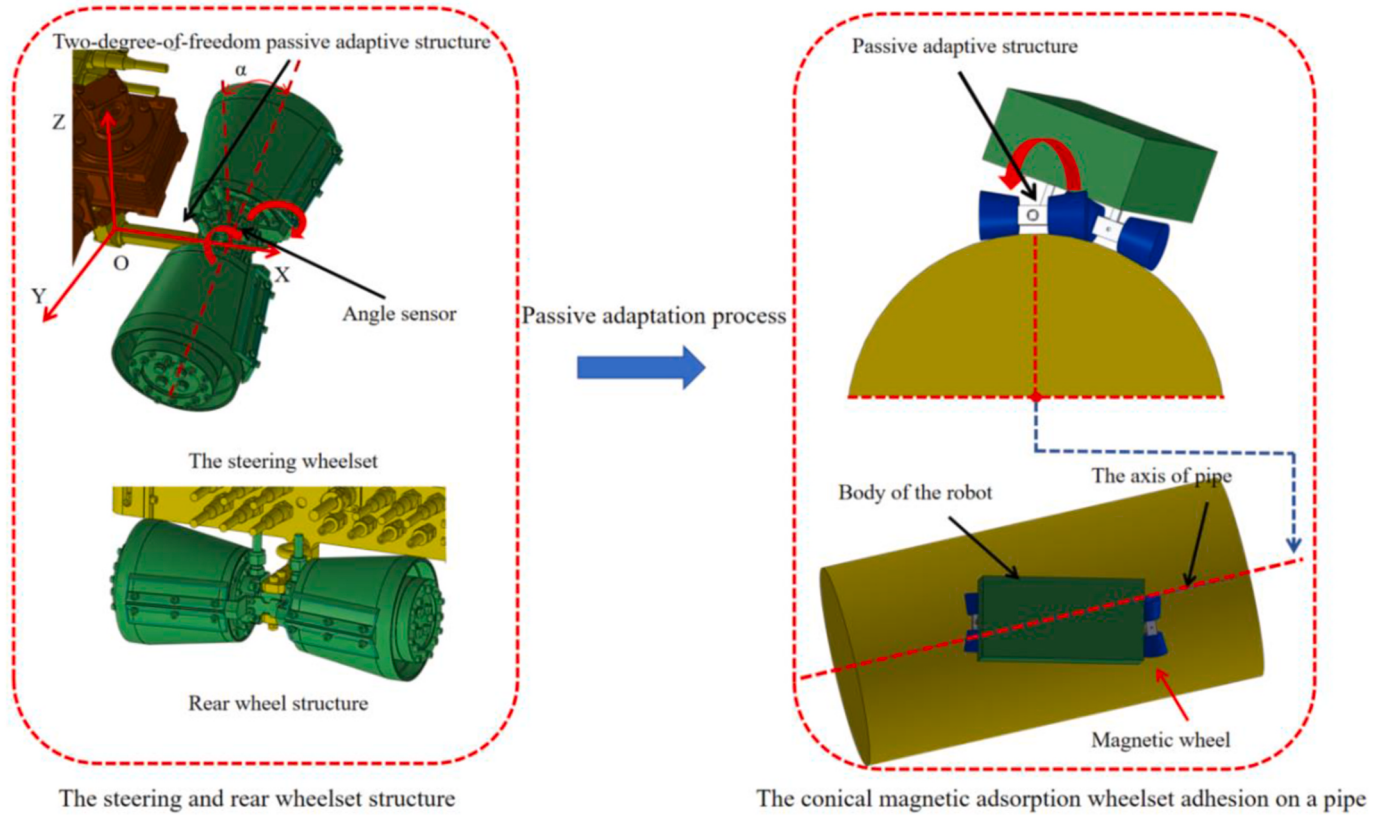


Fig. 2. Robot wheelset structure and passive adaptive motion of the cylindrical structure.

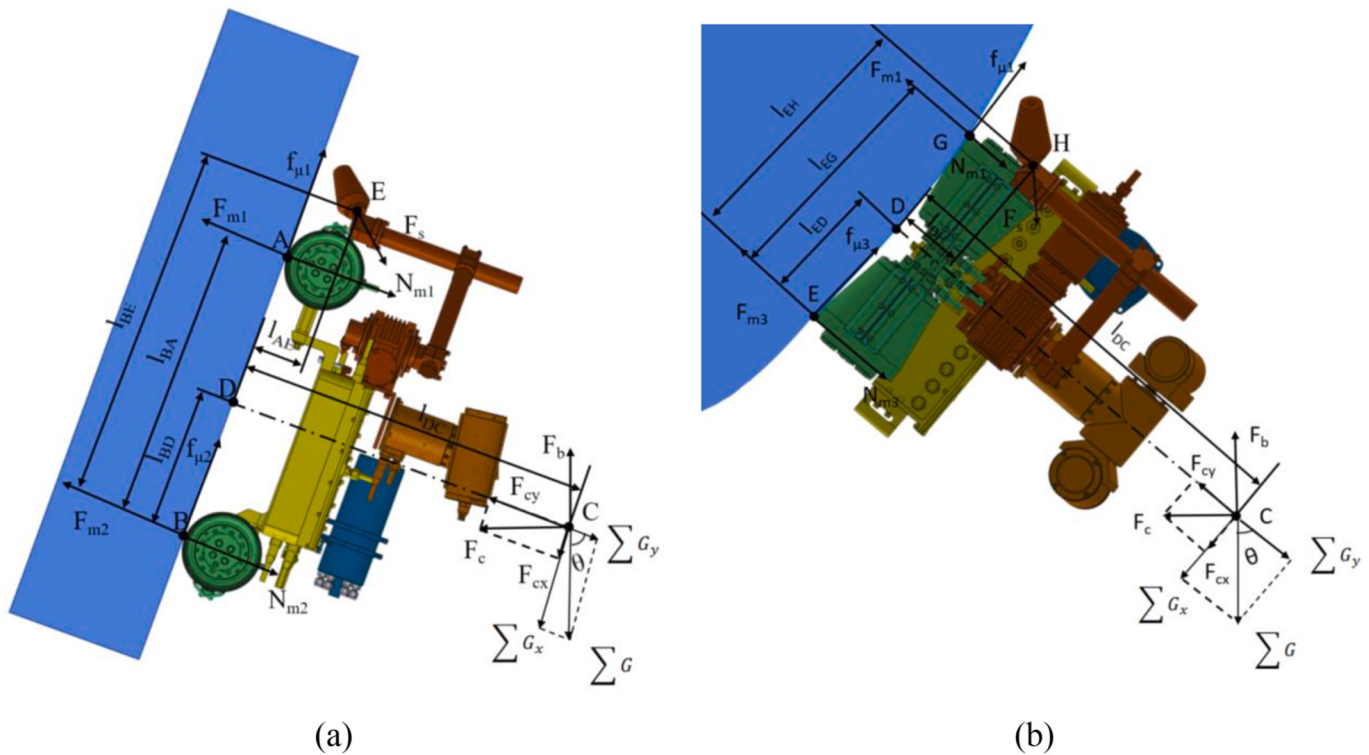


Fig. 3. Static forces analysis of the wall-climbing cleaning robot.

Table 2

The parameters in the static forces analysis.

Symbol	Description	value	Symbol	Description	value
mr	The robot mass	52 kg	ms	Current load	$\rho S_S v_1 \Delta t$
Fm1	Magnetic adsorption force of the right-front wheel	867N	f _{μ1}	Friction on the front wheel (right side)	$\mu N_m 1$
Nm1	Supporting force on the front wheel (right side)	$\frac{1}{4\mu} \sum x$	ΣG	Force in the vertical direction	mrg-Fb
ΣGx	The resultant force in the X-axis direction	(mrg-Fb) $\sin\theta + F_c \cos\theta$	ΣGy	The resultant force in the Y-axis direction	(mrg-Fb) $\cos\theta - F_c \sin\theta$
Fb	The buoyancy of the robot	190.9N	Fc	The ocean current force on the robot	336.3N
Fs	The water jet reaction force	115.9N	lBH	The force arm between Fs and Nm2	0.6m
lAH	The force arm between Fs and f _{μ1}	0.09m	lEH	The force arm between Fs and Nm3	0.36
lBD	The force arm between ΣGy and Nm2	0.26m	lBA	The force arm between Nm1 and Nm2	0.51m
lEG	The force arm between Nm1 and Nm3	0.29m	lDC	The force arm between f _{μ1} and ΣGx	0.15m
V1	The initial velocity of seawater	1.25 m/s	lED	The force arm between ΣGy and Nm3	0.15m
ρ	The density of seawater	$1.025 \times 10^3 \text{ kg/m}^3$	V2	The speed of seawater after impacting on the robot	0 m/s
μ	The friction coefficient	0.18	Ss	The cross-sectional area of the robot	0.21m ²

Table 3

Magnetic properties of sintered NdFeB magnets.

NdFeB magnet	Br (T)	Hcb (kA/m)	BH (kJ/m ³)
N52	1.43–1.48	≥876	398–422

with the wall, the robot must have a structure that ADAPTS to the shape of the wall, such as an elastic suspension, but this leaves the center of gravity of the robot's body unfixed (Eto and Asada, 2020). Therefore, based on the above considerations, the robot structure adopts a split type in this paper, divided into the front and back parts. Two parts are connected through the body in the middle; the front part is a steering wheel set that is driven by two electric motors, while the rear part is the electric motor-driven wheelset, as shown in Fig. 2, a two-degree-of-freedom passive adaptive structure connects the front two steering wheels, so one side can rotate in two directions relative to the other. When the robot moves freely on a cylindrical structure, such as linear motion, turning motion, and even spiral upward motion, the robot's four conical magnetic adsorption wheelset theories can use the two-degree-of-freedom passive adaptive structures to contact the surface of the cylindrical structure.

As shown in Fig. 2, the steering wheelset is connected to the robot body through a two-degree-of-freedom passive adaptive structure, while the rear wheel group is fixed to the robot body through bolts. A coordinate system is established at the connection center of the rotation axis. The robot with O as the origin, the right direction along the rotation axis is the positive direction of the X-axis, and the vertical direction of the X-axis is the positive direction of the Y-axis. The vertical direction is the

positive direction of the Z-axis. The steering wheelset can rotate around the X-axis to passively adapt to different surface curvatures. The steering wheel set can also rotate around the Z-axis for steering, the steering angle $\alpha \in [-20.5^\circ, 20.5^\circ]$, and rotate around the X-axis around $\beta \in [-180^\circ, 180^\circ]$. Fig. 2 is a schematic diagram of the robot's free motion on the circular surface using the passive adaptive structure.

2.2. Magnetic adsorption components

To ensure structural strength, cylindrical structures with different diameters are used on the offshore jacket platform, resulting in sizeable excessive curvature of the wall and a circular arc of varying curvature on the surface. The conventional flat wheel design cannot adapt to the above-wall surface.

To solve the above problems, the conical magnetic adsorption wheelset structure is proposed in this paper. As shown in Fig. 1, the permanent magnet is embedded in the wheel. The magnet and the wall are supported by direct contact between the shell, and the magnet is adsorbed in a non-contact manner. This advantage is that the overall structure of the robot is simple, the weight is light, and each conical magnetic adsorption wheel pair can be driven independently, ensuring the flexible movement of the robot on the steel structure wall and the robot's carrying capacity. Compared with the traditional cylindrical wheel, the advantage is that the overall volume of the magnetic wheel is smaller, the mass is lighter, and the adsorption performance is better.

3. Stability analysis

The boundary conditions for the robot to work on the adsorption wall are as follows:

- Case 1.** The robot can move along the wall without slippage.
- Case 2.** The robot can move along the wall without capsizing.
- Case 3.** The robot can move along the wall without leaning sideways.

According to D'Alembert's principle, for several dangerous states analyzed by static mechanics, the balance equations of the force and moment when the robot moves in a straight line along the steel wall are as follows:

The cylindrical structure is simplified as a camber with a tilt angle ranging from $\theta \in [0, 90^\circ]$, parallel to the horizontal plane to the vertical (see Fig. 3). The total load of the robot on the cylindrical structure surface is simplified as a single force applied to point C (the center of gravity of the robot). The coordinate system is established with point C as the coordinate origin, the x-axis positive direction is downward along the cylindrical structure generatrix, and the y-axis positive direction is vertical to the right with the cylindrical structure generatrix. The robot's parameters are shown in Table 2.

Under the action of the current load, the robot will be impacted to a certain extent (see Table 3). The maximum design current speed is 1.0 m/s for this design. Due to the complexity of the ocean current force, it is simplified as horizontal in the analysis and applied to the robot's center of gravity position. According to the impulse-momentum theorem:

$$F_c = \frac{mv_2 - mv_1}{\Delta t} = -\frac{mv_1}{\Delta t} \quad (3.1)$$

The current load can be expressed as:

$$m_s = \rho v = \rho \int S_S v_1 dt = \rho S_S v_1 \Delta t \quad (3.2)$$

Bring Eq. (3.1) into Eq. (3.2):

$$F_c = -\frac{\rho S_S v_1 \Delta t v_1}{\Delta t} = -\rho S_S v_1^2 \approx 336.3N \quad (3.3)$$

Among them, the water jet reaction force can be calculated by:

$$F_S = 0.745Q\sqrt{P} \quad (3.4)$$

The design value of high-pressure water jet pressure adopted in this paper is $P = 50$ MPa, the flow rate is $Q = 22\text{L}/\text{min}$, and the angle between the nozzle and the horizontal ground is 45° . By substituting each parameter, the reaction force of the water jet is $F_S = 115.9\text{N}$.

For Case 1, the static equilibrium equation in the critical state can be established:

$$\begin{cases} 2F_{m1} + 2F_{m2} = \sum G_y + 2N_{m1} + 2N_{m2} + F_S \cos 45^\circ \\ \sum G_x + F_S \sin 45^\circ \leq 2 \sum f = 2\mu N_{m1} + 2\mu N_{m2} \end{cases} \quad (3.5)$$

Because the motor has a self-locking function, the influence of rolling friction can be ignored. So, μ here refers to its sliding friction coefficient. Therefore, the minimum magnetic adsorption force required is:

$$F_{mm1} \geq \frac{1}{4} \left[\left(m_r g - F_b + \frac{F_c}{\mu} \right) \cos \theta + \left(\frac{m_r g - F_b}{\mu} - F_c \right) \sin \theta + F_S \left(\frac{\sqrt{2}}{2} + \frac{1}{\mu} \frac{\sqrt{2}}{2} \right) \right] \quad (3.6)$$

Because $\theta \in [0, 90^\circ]$, F_{mm1} increases first and then decreases, and the maximum value of 788.2N is obtained at $\theta = \tan^{-1} \frac{1358.6}{546.8} = 33.4^\circ$. At $\theta = 0^\circ$, the robot is parallel to the horizontal plane and adsorbed on the wall. At this time, F_{mm1} is 681.1N . At $\theta = 90^\circ$, the robot is perpendicular to the horizontal plane and adsorbed on the wall. At this time, F_{mm1} is 492.9N .

Case 2 is the critical state of overturning around the lower half due to the torque generated by the load, and the necessary torque state equation can be established now.

$$2F_{m1}l_{BA} - 2N_{m1}l_{BA} - \sum G_y l_{BD} - \sum G_x l_{DC} - F_S \cos 45^\circ l_{AH} - F_S \sin 45^\circ l_{BH} = 0 \quad (3.7)$$

In the critical case, the normal force on all contacts except the rotating shaft is zero, and the mechanical equation of the minimum magnetic adsorption force can be obtained:

$$F_{mm2} = \left[\frac{(l_{DC} + l_{BD})(m_r g - F_b)}{2l_{BA}} \right] \cos \theta + \frac{(l_{DC} + l_{BD})}{2l_{BA}} F_c \sin \theta + \frac{\sqrt{2}}{4l_{BA}} F_S (l_{AH} + l_{BH}) \quad (3.8)$$

In the same way as Eq. (3.6), because $\theta \in [0, 90^\circ]$, F_{mm2} firstly increases and then decreases, and when the maximum value 241.6N is obtained at $\theta = \tan^{-1} \frac{135.2}{128.1} = 45.3^\circ$.

$$\begin{cases} F_{mm2} = 183.5\text{N}, \theta = 0^\circ \\ F_{mm2} = 190.6\text{N}, \theta = 90^\circ \end{cases} \quad (3.9)$$

Similarly, for Case (3), corresponding to Fig. 5(b), the right half part falls off due to the torque generated by the load, and the critical state of overturning around the left half part can be established.

$$2F_{m1}l_{EG} - 2N_{m1}l_{EG} - \sum G_y l_{ED} - \sum G_x l_{DC} - F_S \sin 45^\circ l_{EH} - F_S \cos 45^\circ l_{DH} = 0 \quad (3.10)$$

Similarly, in the critical case, the normal force on all contacts except the rotating shaft is zero, and the mechanical equation of the minimum magnetic adsorption force is obtained:

$$F_{mm3} = \left[\frac{(l_{DC} + l_{ED})(m_r g - F_b)}{2l_{EG}} \right] \cos \theta + \frac{(l_{DC} + l_{ED})}{2l_{EG}} F_c \sin \theta + F_S \frac{\sqrt{2}}{4l_{EG}} (l_{EH} + l_{AH}) \quad (3.11)$$

In the same way as Eq. (3.8), because $\theta \in [0, 90^\circ]$, F_{mm3} firstly increases

and then decreases, and when the maximum value is 239.6N is obtained at $\theta = \tan^{-1} \frac{173.9}{164.8} = 46.7^\circ$.

$$\begin{cases} F_{mm3} = 241.1\text{N}, \theta = 0^\circ \\ F_{mm3} = 250.2\text{N}, \theta = 90^\circ \end{cases} \quad (3.12)$$

Received:

$$F_{mmn} = \max(F_{mm1}, F_{mm2}, F_{mm3}) \quad (3.13)$$

In summary, each wheel's minimum magnetic adsorption force is 867N after taking 1.1 times as the safety factor.

4. Permanent magnet wheel design and magnetic field simulation analysis

4.1. Theoretical calculation of magnetic adsorption force

The adsorption mechanism is the critical component of a wall-climbing cleaning robot. The performance of the magnetic wheel can be improved by optimizing the magnetic circuit of the magnetic wheel. According to Maxwell's equations, the differential forms of magnetic field intensity H and magnetic induction intensity B are as follows:

$$\begin{cases} \nabla \times H = J \\ \nabla \cdot B = 0 \\ B = \mu H \end{cases} \quad (4.1)$$

In the formula: J —electric field density, A/m^2 ;

μ —permeability of the medium.

The vector magnetic potential A is introduced to simplify the problem. To realize the uniqueness of A , according to the Coulomb specification, there are:

$$B = \nabla \times A \quad (4.2)$$

$$\nabla \cdot A = 0 \quad (4.3)$$

According to Eqs. (4.1) - (4.3), the equivalent double curl equation of vector magnetic potential function can be obtained:

$$\nabla \times \frac{1}{\mu} \nabla \times A = J \quad (4.4)$$

The Eq. (4.2) can be obtained as follows:

$$\begin{cases} B_x = \frac{\partial A_z}{\partial y} - \frac{\partial A_y}{\partial z} \\ B_y = \frac{\partial A_x}{\partial z} - \frac{\partial A_z}{\partial x} \\ B_z = \frac{\partial A_y}{\partial x} - \frac{\partial A_x}{\partial y} \end{cases} \quad (4.5)$$

In the rectangular coordinate system, Eq. (4.4) can be expanded as:

$$\begin{cases} \frac{\partial}{\partial y} \left(\frac{1}{\mu} \right) \left(\frac{\partial A_y}{\partial x} - \frac{\partial A_x}{\partial y} \right) - \frac{\partial}{\partial z} \left(\frac{1}{\mu} \right) \left(\frac{\partial A_x}{\partial z} - \frac{\partial A_z}{\partial x} \right) - \frac{1}{\mu} (\nabla^2 A)_x = J_x \\ \frac{\partial}{\partial z} \left(\frac{1}{\mu} \right) \left(\frac{\partial A_z}{\partial y} - \frac{\partial A_y}{\partial z} \right) - \frac{\partial}{\partial x} \left(\frac{1}{\mu} \right) \left(\frac{\partial A_y}{\partial x} - \frac{\partial A_x}{\partial y} \right) - \frac{1}{\mu} (\nabla^2 A)_y = J_y \\ \frac{\partial}{\partial x} \left(\frac{1}{\mu} \right) \left(\frac{\partial A_x}{\partial z} - \frac{\partial A_z}{\partial x} \right) - \frac{\partial}{\partial y} \left(\frac{1}{\mu} \right) \left(\frac{\partial A_z}{\partial y} - \frac{\partial A_y}{\partial z} \right) - \frac{1}{\mu} (\nabla^2 A)_z = J_z \end{cases} \quad (4.6)$$

In Eqs. (4.2) - (4.4), $A_x, A_y, A_z, B_x, B_y, B_z, J_x, J_y$, and J_z are the components of B, H in the x, y , and z directions in the Cartesian coordinate system, respectively. From the actual situation of the analyzed magnetic field and the boundary conditions of the magnetic field, Eq. (5.6) is finally obtained.

$$F = \oint_S T dS = \oint_S \left[\frac{1}{\mu} (B \cdot n) B - \frac{1}{2\mu} B^2 n \right] dS = \frac{1}{2\mu} \oint_S B^2 n dS \quad (4.7)$$

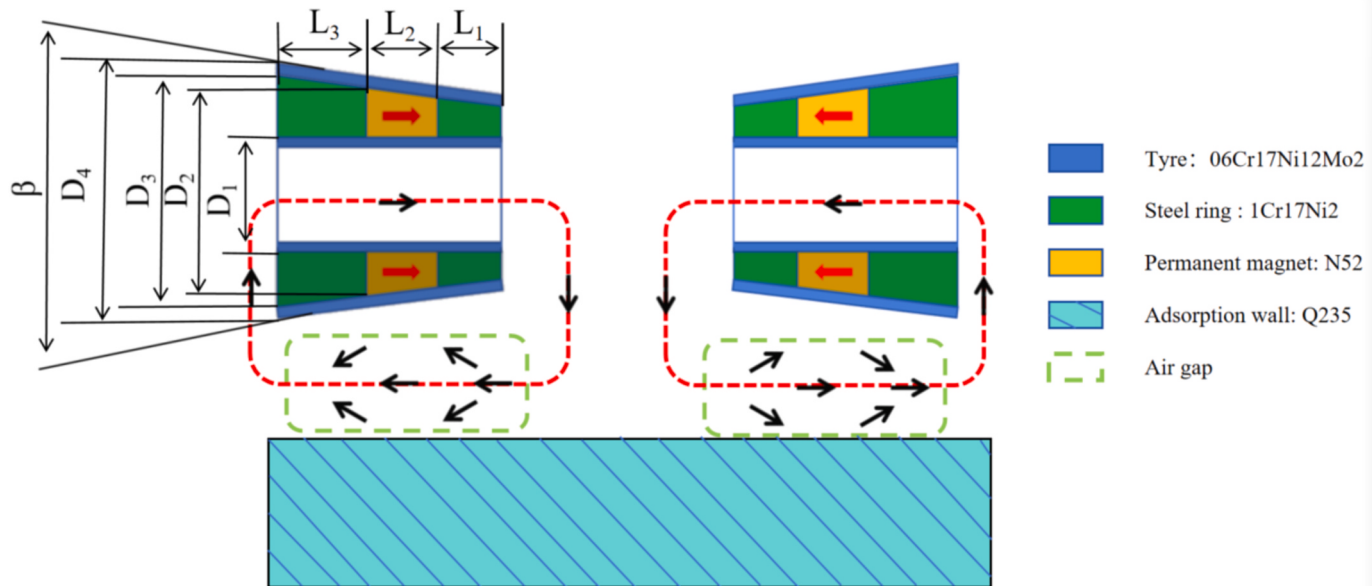


Fig. 4. Distribution of magnetic field lines generated by permanent magnets.

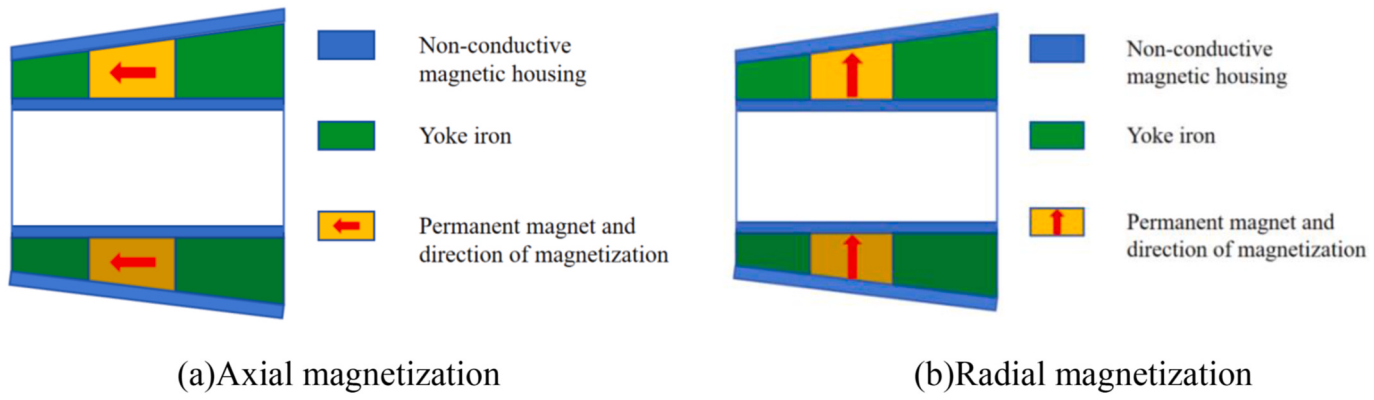


Fig. 5. Two kinds of magnetic circuits designed.

In the formula: S -air gap;

n -the unit vector of the outer average direction of area dS ;

It can be seen from Eq. (4.7) that the air gap on the closed surface S has the most significant influence on the magnetic adsorption force.

4.2. Design and analysis of magnetic circuit

The conical magnetic adsorption wheelset used for the robot usually consists of three parts: a central ring magnet made of NdFeB, two steel rings glued to both sides of the central ring magnet, and an outer knurled tire made of aluminum alloy. The magnetization direction of the two-wheel magnets is opposite, which improves the utilization rate of the magnets, as shown in Fig. 4.

As shown in Fig. 5, two magnetic circuits are designed according to the relative position relationship among the neutral surface of the permanent magnet, the magnet, and the air gap.

Fig. 5(a) adopts the axial magnetization scheme, and Fig. 5(b) adopts the radial magnetization scheme. Figs. 6 and 7 are the simulation tests of the two magnetization schemes.

Under the axial magnetization scheme, the maximum magnetic adsorption force is 726.2 N, and the maximum magnetic field strength is 7.525T. Under the radial magnetization scheme, the maximum adsorption force is 378.7 N, and the maximum magnetic field strength is

10.146T. The difference between axial magnetization and radial magnetization. This difference is because the radial magnetization loop is long, and there is a significant magnetic flux leakage. In contrast, the experimental prototype adopts the scheme of axial magnetization.

4.3. Adhesion force analysis

The permanent magnet and the cylindrical structure are mathematically modeled. Because they are axisymmetric entities, only the first and fourth quadrants are analyzed, as shown in Fig. 8.

The tangent point between the permanent magnet and the outer wall is $P_1 (X_1, Y_1)$. The vertex of the small terminal face in the fourth quadrant is $P_2 (X_2, Y_2)$. The vertex of the sizeable terminal face in the fourth quadrant is $P_3 (X_3, Y_3)$. The radius of the large terminal face of the permanent magnet is R_1 , the radius of the small terminal face of the permanent magnet is R_2 , and the radius of the outer wall is R_3 .

Let d be the distance between the permanent magnet micro-element and the cylindrical structure, then the air gap S_K is:

$$S_K = \sum_{i=1}^{x_3-x_2} d_i \quad (4.8)$$

Using the Newton-Leibniz formula, the vertical line of point P_2 intersects with the cylindrical structure at point $P_6 (X_6, Y_6)$, and the

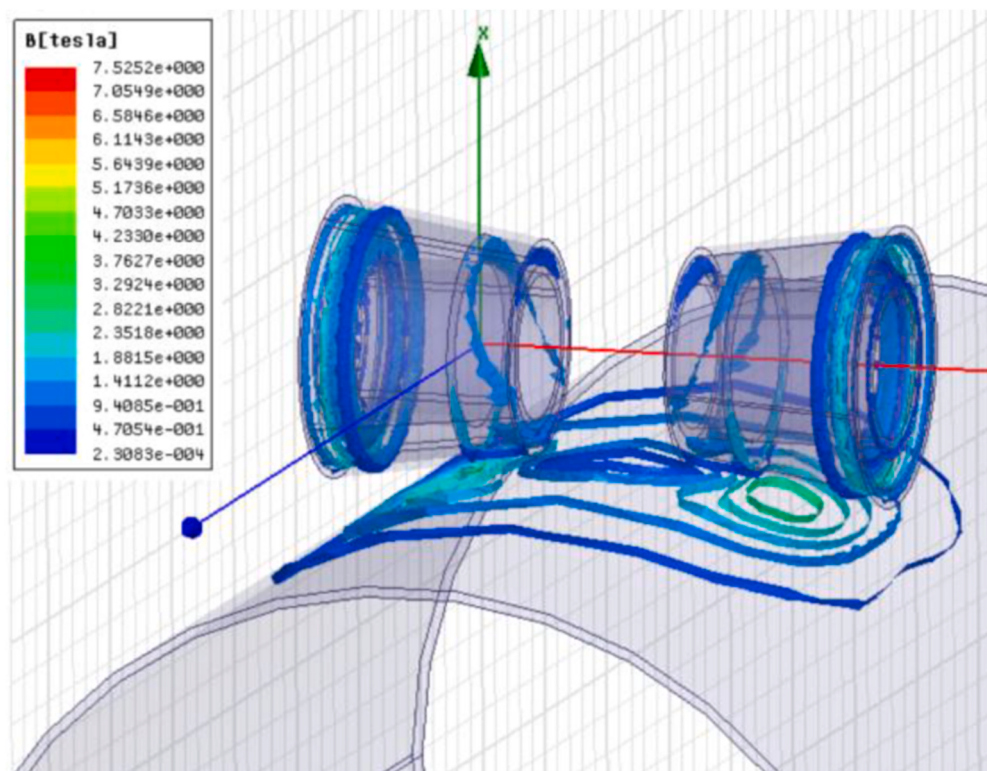


Fig. 6. Axial magnetization magnetic field cloud diagram.

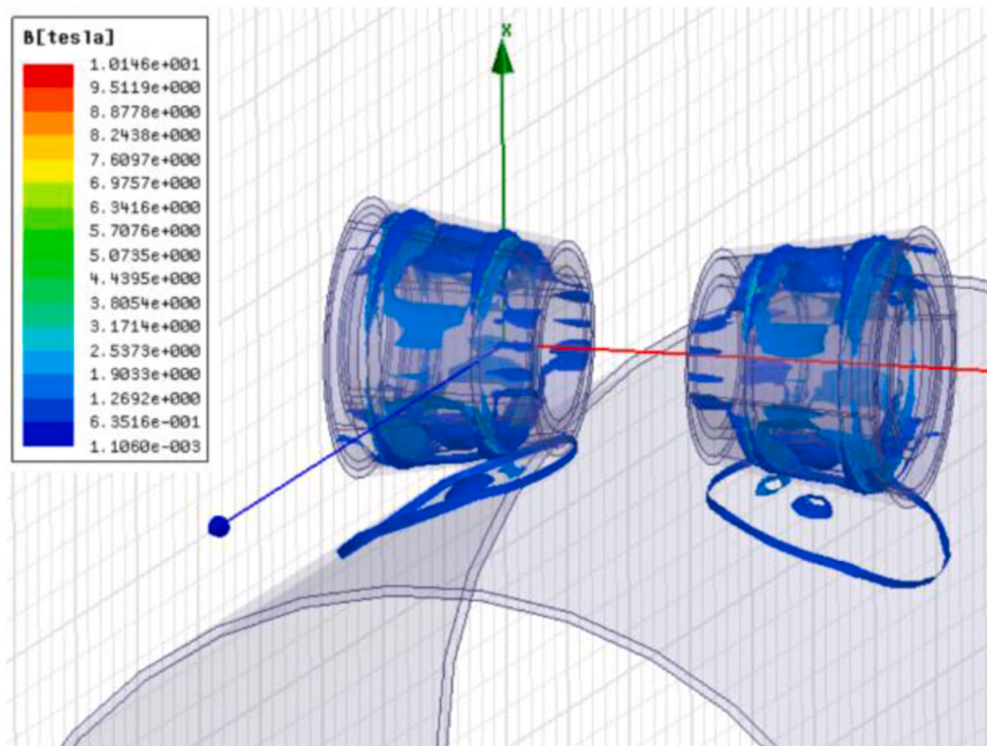


Fig. 7. Radial magnetization magnetic field cloud diagram.

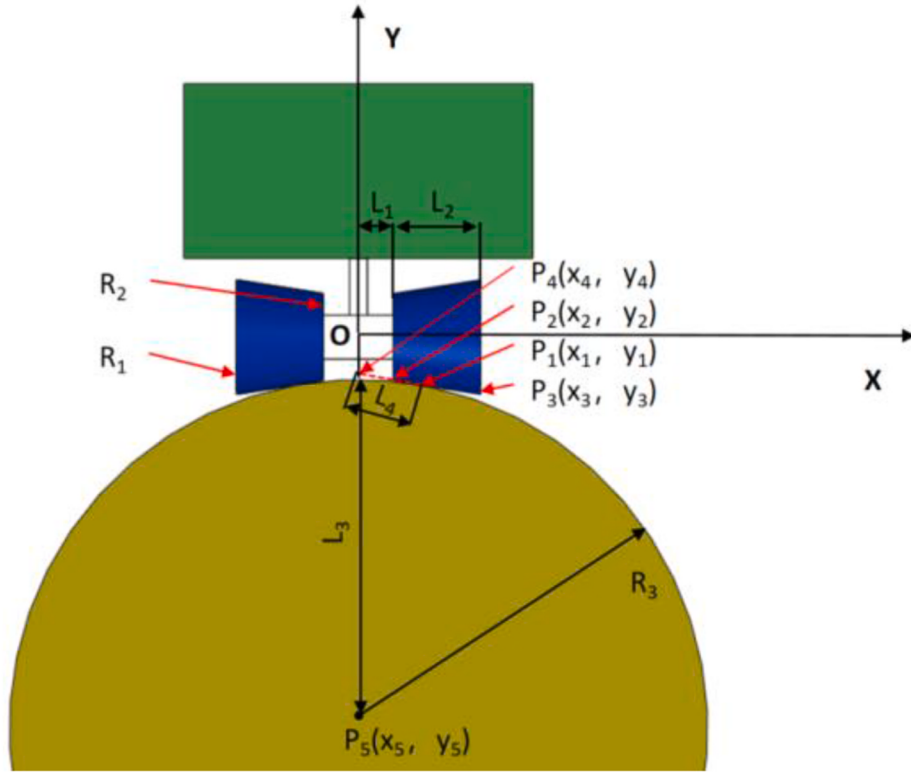


Fig. 8. The mathematical modeling of the permanent magnet and the cylindrical structure.

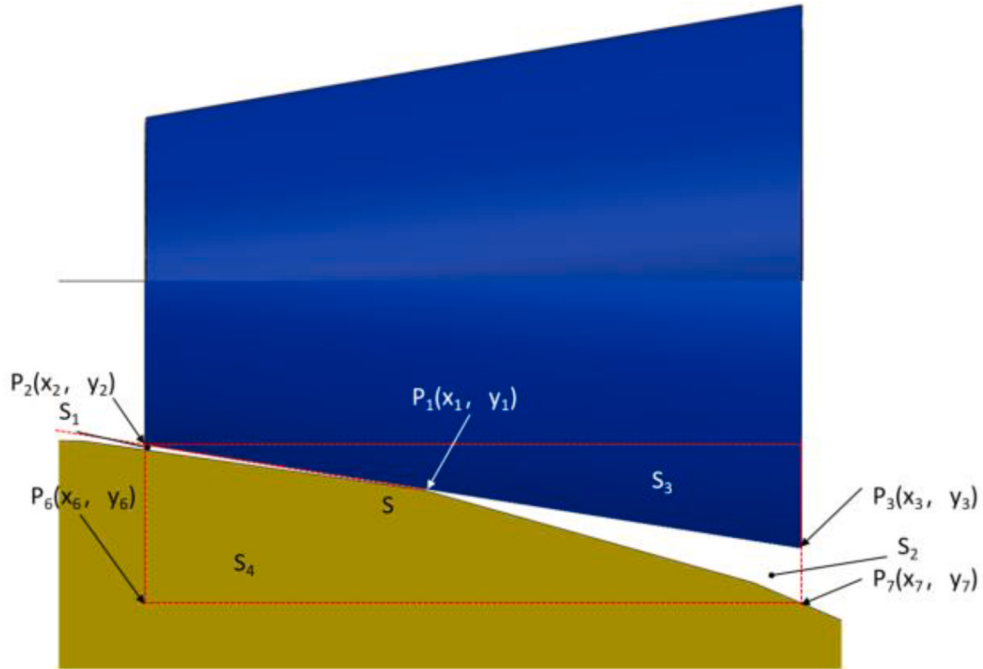


Fig. 9. Contact surface.

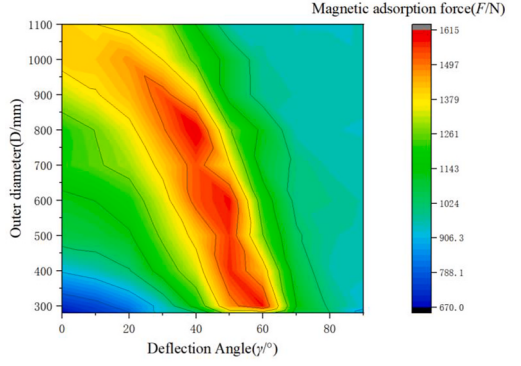
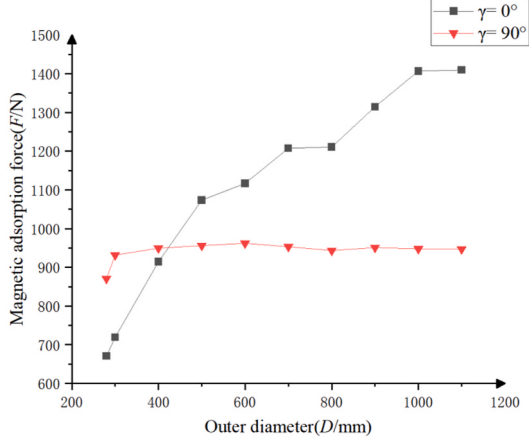
vertical line of point P_3 intersects with the cylindrical structure at point $P_7(X_7, Y_7)$. S is the rectangular area between P_2 , P_3 , P_6 , and P_7 , and S_1 and S_2 are the sum of the air gap between the conical magnetic adsorption wheelset and the adsorption surface, then:

$$S_k = \sum_{i=1}^{X_3-X_2} d_i = S - S_3 - S_4 \quad (4.9)$$

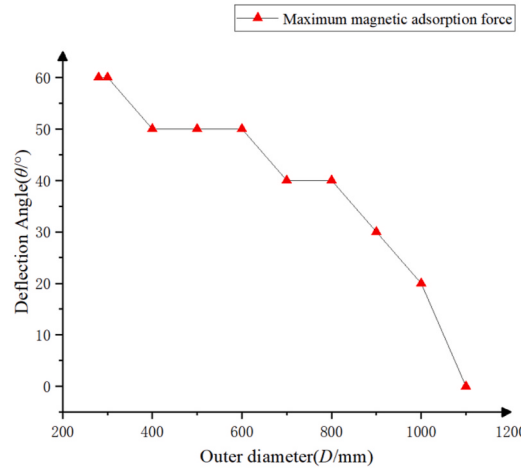
It is known that the line segment $L_{P_2P_3}$ function between points P_2 and P_3 is expressed as:

$$L_{P_2P_3} : \frac{X - X_1}{X_2 - X_1} = \frac{Y - Y_1}{Y_2 - Y_1} \quad (4.10)$$

Then the coordinate values of $P_4(0, -Y_4)$ and $P_5(0, -Y_5)$ are obtained:

(a) The variation trend of magnetic adsorption force F with D and γ 

(b) The variation trend of the magnetic adsorption force with the diameter of the cylindrical structure



(c) The variation trend of the maximum magnetic adsorption force of the conical magnetic adsorption wheelset with the cylindrical structure diameter

Fig. 10. Analysis of the variation trend of magnetic adsorption force F .

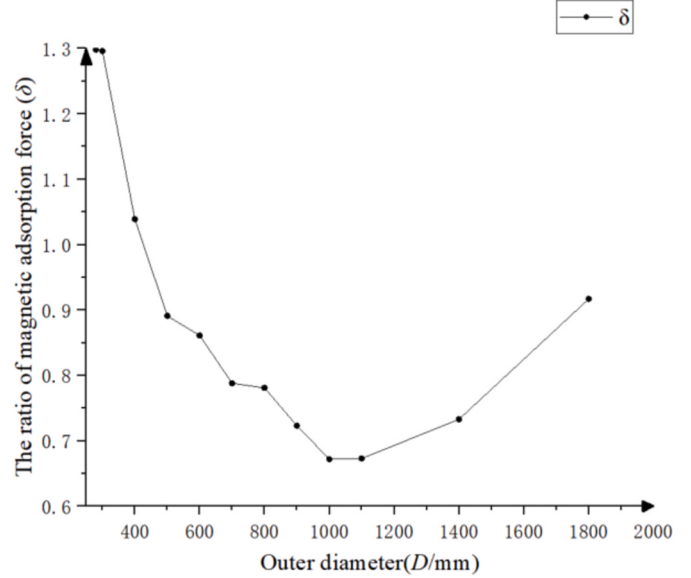
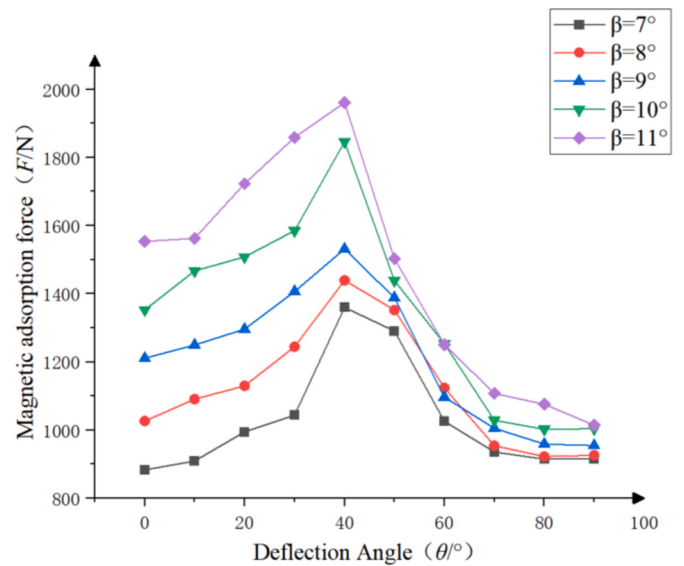
$$\begin{cases} Y_4 = \frac{-X_1(Y_2 - Y_1)}{X_2 - X_1} + Y_1 \\ Y_5 = Y_4 + L_3 \end{cases} \quad (4.11)$$

L_3 is the distance between points P_4 and P_5 :

$$L_3 = \sqrt{R_3^2 + X_1^2 + (Y_4 - Y_1)^2} \quad (4.12)$$

Then, the cylindrical structure function expression is obtained:

$$R_3^2 = X^2 + (Y + Y_5)^2 \quad (4.13)$$

**Fig. 11.** The variation of δ with cylindrical structure diameter D .**Fig. 12.** Angle-offset magnetic adsorption force at different cone angles.

The coordinate values of P_6 and P_7 points are obtained, and the air gap area is finally calculated as follows:

$$S_k = Y_7 L_2 - \frac{1}{2} (Y_3 - Y_2) L_2 - \int_{X_2}^{X_3} dx \int_{-Y_5}^{\sqrt{R^2 - x^2} - Y_5} dy \quad (4.14)$$

Substituting $X_2 = L_1$, $X_3 = L_1 + L_2$, $Y_2 = R_1$, $Y_3 = R_2$, $R_2 = R_1 + L_2 \tan \alpha$ into simplification, we can get:

$$S_k = L_2 \left[3 \left(\frac{X_1(Y_1 - r_1)}{X_1 - L_1} - Y_1 - \sqrt{R_3^2 + X_1^2 + \frac{X_1^2(Y_1 - R_1)^2}{(X_1 - L_1)^2}} \right) - \frac{1}{2} (L_2 \tan \alpha) \right] +$$

$$\frac{2L_1[R_3^2 - (L_1 + L_2)^2]^{\frac{3}{2}} - (L_1 + L_2)(R_3^2 - R_1^2)^{\frac{3}{2}}}{2(L_1 + L_2)L_1} \quad (4.15)$$

The tangent point P_1 (X_1 , Y_1) satisfies the equation:

$$Y_1 = (X_1 - L_1) \tan \alpha + R_1 \quad (4.16)$$

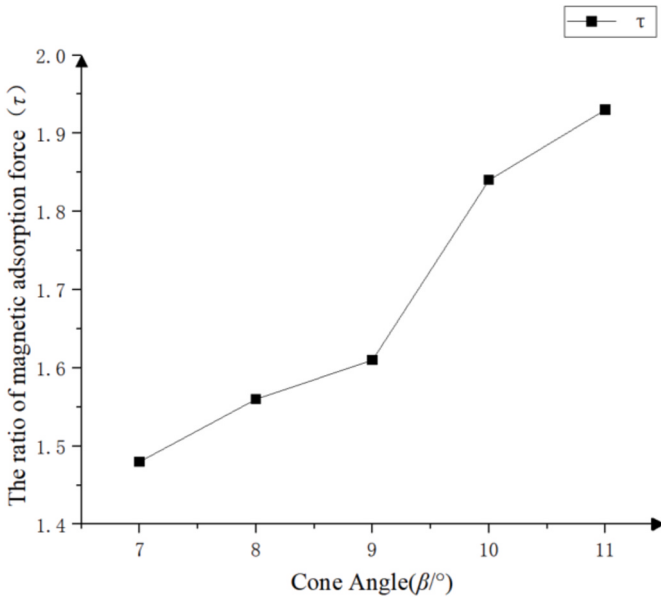


Fig. 13. The variation of τ value at different cone angles.

In summary, can be obtained:

$$S_k = -L_2 \left[3 \left(\sqrt{R_3^2 + X_1^2 (1 + \tan \alpha^2)} \right) + \frac{1}{2} (L_2 \tan \alpha) \right] + \frac{2L_1 [R_3^2 - (L_1 + L_2)^2]^{\frac{3}{2}} - (L_1 + L_2)(R_3^2 - R_1^2)^{\frac{3}{2}}}{2(L_1 + L_2)L_1} - 3R_1L_1 \quad (4.17)$$

Among them, L_1 , R_1 , R_3 , and L_2 are fixed values, and the variable is cone angle α . To facilitate the intuitive representation of the influence of variables, the original formula can be transformed into:

$$S_k = -L_2 \left[3 \left(\sqrt{R_3^2 + X_1^2 (1 + \tan \alpha^2)} \right) + \frac{1}{2} (L_2 \tan \alpha) \right] + t \quad (4.18)$$

Here, t are constants related to L_1 , R_1 , R_3 , and L_2 . From this formula, it can be intuitively obtained that the air gap S_k decreases with the

Table 4
Structural parameters of the conical magnetic adsorption wheelset.

Parameter	Value
L_1	30 mm
L_2	50 mm
L_3	20 mm
D_1	80 mm
D_2	127.88 mm
D_3	135.66 mm
D_4	143.76 mm
β	9°

Table 5
Main parameters of the robot.

Attributes	Parameter
Dry weight	52 kg
Load Capacity	≤ 109 kg
Maximum speed	0.5 m/s
overall size	782*497*326 mm
Mode of communication	RS485/CAN
Cleaning method	Ultra-high-pressure water jet/cavitation jet

increase of the cone angle, and the magnetic adsorption force is the opposite.

Bring Eq. (4.18) into Eq. (4.7); the magnetic adsorption force can be expressed as:

$$F = \frac{1}{2\mu_0 J_S} \oint B^2 ds = 2 \sum_{i=1}^n \frac{B_i^2 S_k}{2\mu_0} \quad (4.19)$$

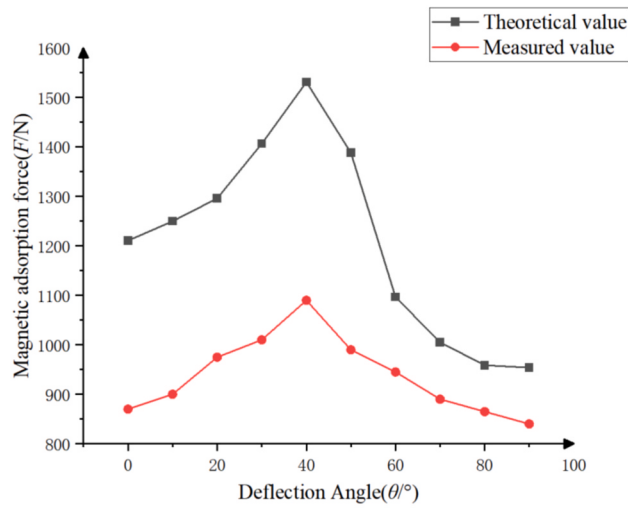
In the formula, B_i represents the magnetic induction intensity of the permanent magnet; S_k represents the effective force area of each equal air gap.

If other parameters are unchanged when the magnetic wheelset changes the angle between its axis and the cylindrical structure axis, the air gap $\oint ds$ changes in a single decrease (see Fig. 9).

The simulation solution is shown in Fig. 10, where D is the diameter of the cylindrical structure and γ is the angle between the axis of the conical magnetic adsorption wheel and the axis of the cylindrical



(a) Magnetic adsorption force experiment



(b) Simulated results and experimental results

Fig. 14. Comparison of simulated results and experimental results.

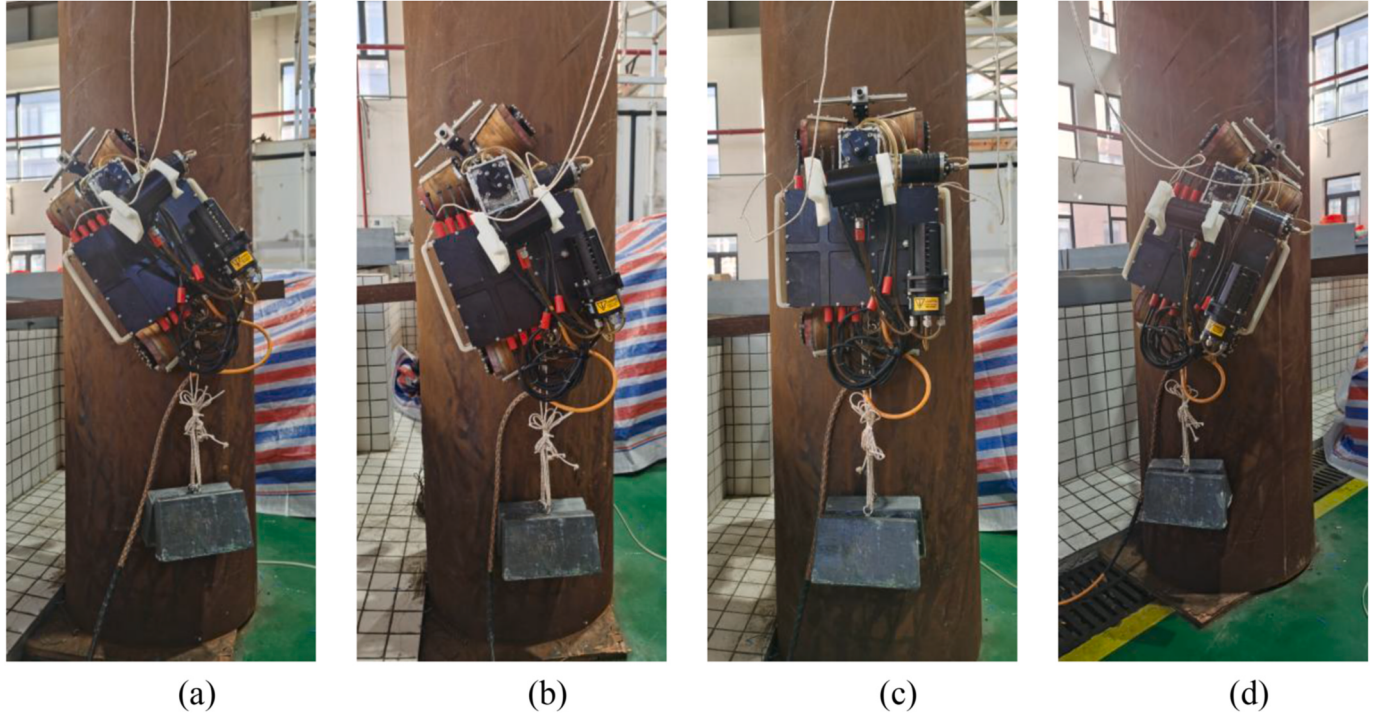


Fig. 15. Load test diagram of the wall-climbing robot on the cylindrical steel structure: (a ~ d): Freely Motion of Robot in Loaded State.



Fig. 16. Traction test of robot.

structure.

The conical magnetic adsorption wheel rotates on the wall of cylindrical structures with different diameters and a thickness of 5 mm. The minimum diameter D of these cylindrical structures is 280 mm, and the maximum is 1100 mm. The rotation motion of the conical magnetic adsorption wheel starts with the axis of the conical magnetic adsorption wheel perpendicular to the axis of the cylindrical structure, at this time $\gamma = 0^\circ$, and ends with the axis of the conical magnetic adsorption wheel parallel to the axis of the cylindrical structure, at this time $\gamma = 90^\circ$. In the

Table 6
Traction experimental data.

Wall condition	Dead weight (kg)	peak traction (kg)	Magnetic adsorption force (kg)	Friction coefficient
Dry environment	52	131	174	0.75
Moist environment	30	34.8	174	0.2

whole process, the variation trend of magnetic adsorption force is shown in Fig. 10. As shown in Fig. 10(b) and (C), with the diameter of the cylindrical structure increasing, the maximum value of magnetic adsorption force shows an increasing trend. In contrast, the minimum value of magnetic adsorption force increases first and then tends to be stable, but the maximum position γ of magnetic adsorption force shows a downward trend. Due to the decrease in the air gap area between the conical magnetic wheelset and the cylindrical structure, the magnetic field strength is enhanced, and the magnetic adsorption force also shows an upward trend.

Here, δ is the ratio of the magnetic adsorption force at $\gamma = 0^\circ$ and $\gamma = 90^\circ$. It can be seen from Fig. 11 that when other parameters remain unchanged, increasing the cylindrical structure's diameter, δ first decreases and then increases, and δ obtains the minimum value at $D = 1000$ mm. Finally, when the cylindrical structure's diameter is infinite, the value of δ should be 1.0 when it is a plane. When the adsorption surface is a plane, the conical magnetic adsorption wheelset rotates at any angle, and the air gap between the conical magnetic adsorption wheelset and the adsorption surface is a fixed value.

Under the plane with the same thickness of 5 mm as the cylindrical structure, the magnetic adsorption force of the conical magnetic adsorption wheelset is 1223.6N, and the magnetic field intensity is 3.3T. From Figs. 10 (c) and Fig. 11, it can be seen that as the diameter of the cylindrical structure tends to infinity, which tends to be a plane, The γ value corresponding to the maximum magnetic adsorption force F_{max} tends to 0° , and the ratio of the magnetic adsorption force of $\gamma = 0^\circ$ and γ

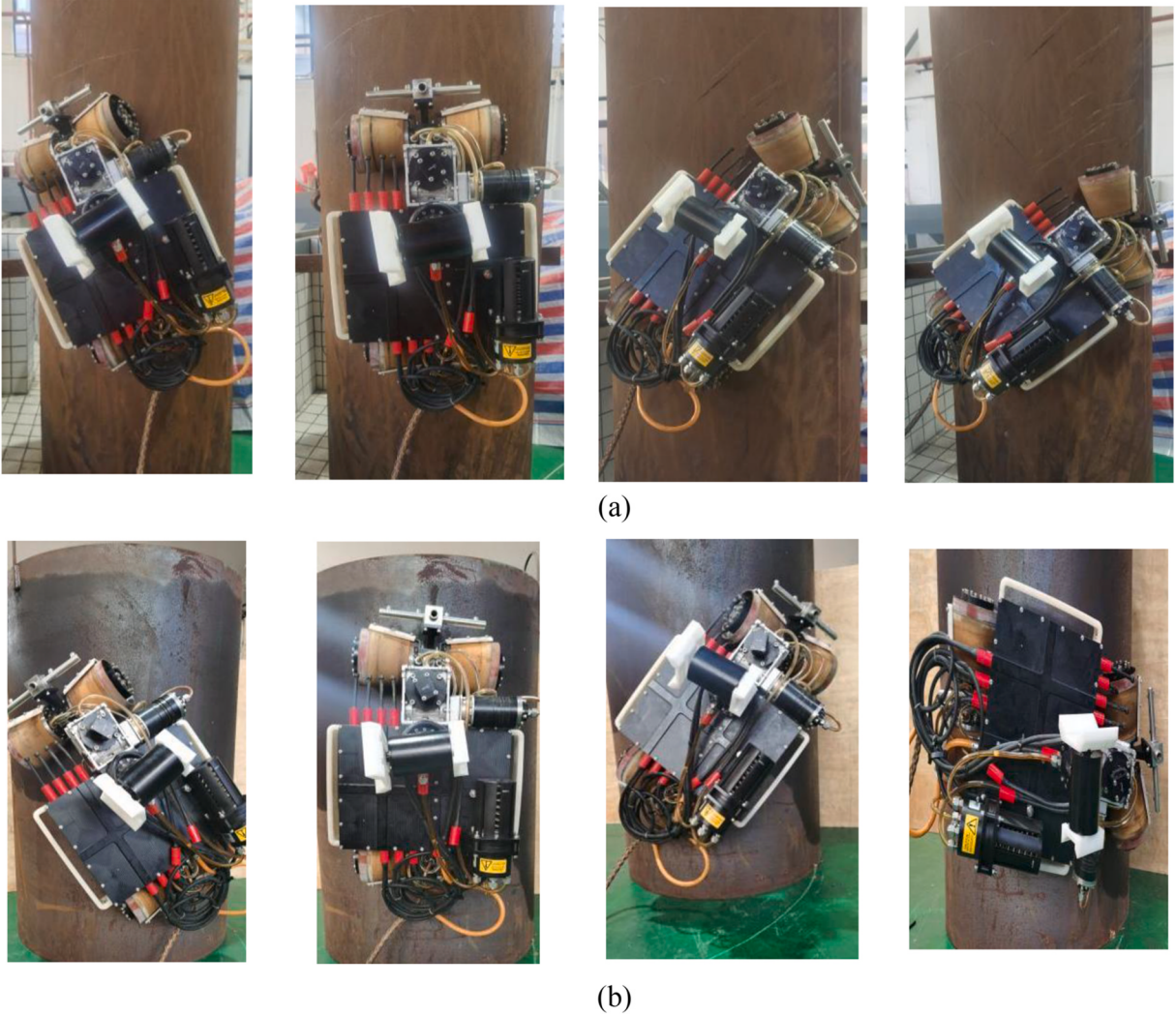


Fig. 17. The robot moves freely on cylindrical steel structures with different diameters: (a) the diameter is 600 mm; (b) 750 mm in diameter.

$= 90^\circ$ increases rapidly and then slowly tends to 1.

The conical magnetic adsorption wheelset offers advantages over the conventional cylindrical wheel when adhering to the cylindrical structure. Firstly, the conical magnetic adsorption wheelset is smaller than the cylindrical wheel under the same maximum diameter, enabling a lightweight design for the entire wall-climbing cleaning robot. Secondly, when adsorbed onto the cylindrical structure, the conical magnetic adsorption wheelset experiences a more excellent attenuation of magnetic force compared to the cylindrical wheel at a 90° angle due to the wheel body's cone angle design. This makes it more conducive to peeling off the wall.

5. Surface adaptability optimization of magnetic adsorption component

The conical magnetic adsorption wheelset's reliability should be manageable simultaneously; otherwise, it will reduce the robot's mobility and cause the problem of stripping off the adsorption wall. It can be seen from Eq. (5.19) that the parameter that affects the magnetic adsorption force is the air gap. The conventional magnetic adsorption wheelset's design is to adapt to the cylindrical structure with different curvatures. Secondly, to make the magnetic adsorption force as small as possible at a certain angle while ensuring the robot's reliable adsorption when the conical magnetic adsorption wheelset changes the angle between its axis and the cylindrical structure axis. The expression of the

ratio is:

$$\tau = F_{mm2}/F_{mm1} \quad (5.20)$$

F_{mm1} is the maximum magnetic adsorption force obtained when the conical magnetic adsorption wheelset rotates on the cylindrical structure, and F_{mm2} is the minimum magnetic adsorption force during the wheel's movement.

The purpose of optimizing the conical magnetic adsorption wheelset is to optimize the cone angle to obtain the most suitable value under the condition of a particular distribution of permanent magnets. By controlling the variables, the variation trend of the magnetic adsorption force of the conical magnetic adsorption wheel at different cone angles is compared and analyzed with the adsorbed cylindrical structure parameters as the quantity and the rotation angle as the variable.

Figs. 12 and 13 show that the cone angle continuously increases, as do the F_{max} and τ values. The variation trend is consistent with the mathematical model obtained by Eq. (5.18). Considering the robot's mobility and the simplicity of disassembly in a non-working state, the cone angle is 9° .

The adsorption force between the magnetic adsorption component and the cylindrical structure under various rotation angles is obtained through the above simulation optimization calculation. At the same time, the magnetic adsorption forces of the conical magnetic adsorption wheelset were measured using the force meter.

The cylindrical steel structure's material is Q235, with a thickness of

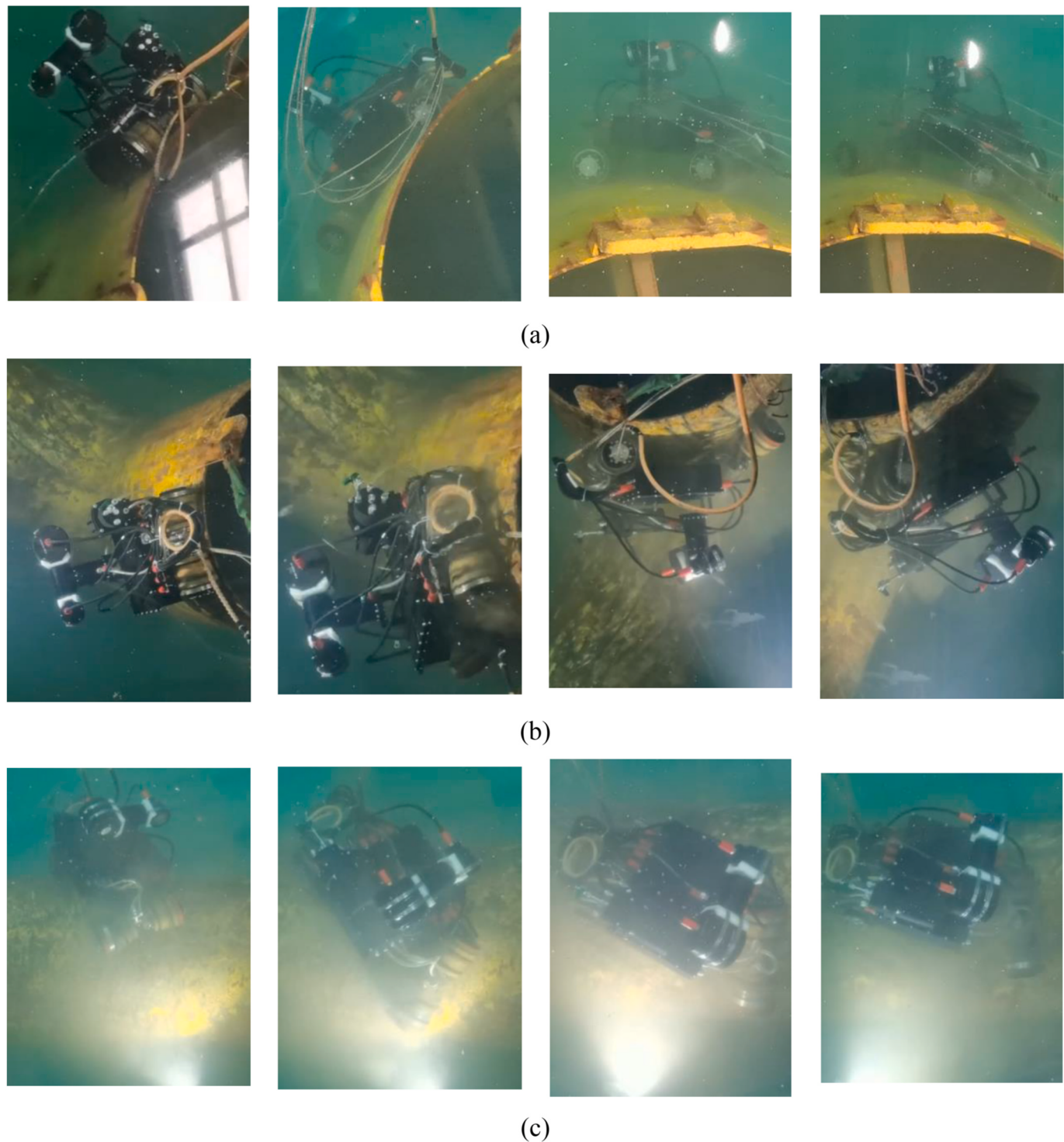


Fig. 18. The robot moves freely on the underwater cylindrical steel structure: (a) Diameter 1800 mm; (b) Diameter 1000 mm; (c) Diameter 900 mm.

5 mm and a diameter of 750 mm. Fig. 14 compares the simulated results with the experimental results.

According to the data comparison, the variation trend of the simulated value is the same as the experimental value, and the experimental values are smaller than those of the simulation. This is because the simulation value is obtained under the ideal boundary condition. The experimental value of the adsorption force of the conical magnetic adsorption wheelset is lower than the simulated value, and there is a machining error in the manufacturing process. For example, the thickness of the polyurethane rubber sleeve cannot guarantee high accuracy,

thereby increasing the air gap and causing its magnetic adsorption force to become smaller. Since the ratio of the measured value to the theoretical value changes in a small range, in the actual design, a coefficient n can be introduced to modify the theoretical value to judge the exact value of the magnetic adsorption force and assist the design and manufacture of the wall-climbing cleaning robot. As shown in Fig. 14, n is 0.71–0.88, with a mean value of 0.80 (see Table 4).



(a) High-pressure water cleaning test with a pressure of 50 MPa and flow rate of 22 L/min

(b) Cavitation jet cleaning test with a pressure of 20 MPa and a flow rate of 67 L/min

Fig. 19. Atmospheric cleaning test.



Fig. 20. Underwater cleaning test.

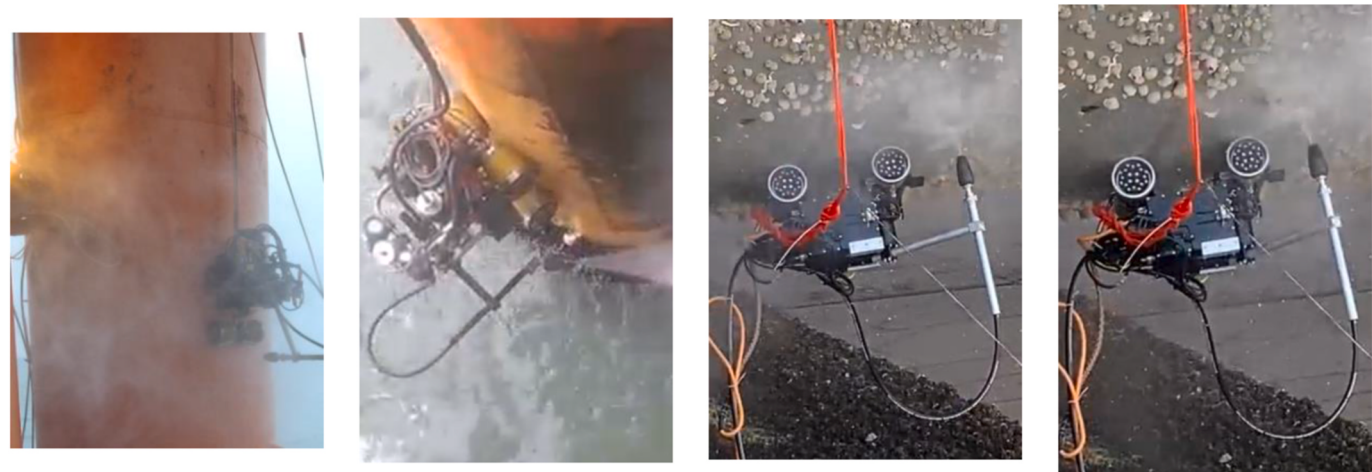


Fig. 21. The robot's cleaning test is carried out on the offshore platform.

6. Experimental verification analysis

Because the theoretical analysis and calculation of magnetic adsorption force efficiently produce a specific deviation from the actual situation, we also need to measure the adsorption performance of the robot further through experiments to verify the variation trend of magnetic adsorption force. This paper combines the conical magnetic adsorption wheelset, passive adaptive structure, and cleaning unit to design and manufacture a magnetic adsorption wall-climbing cleaning robot for offshore jacket platforms that can adapt to the large curvature of the cylindrical structure. The main parameters of the robot are shown in Table 5.

6.1. Conical magnetic adsorption wheelset performance experiment

To test the stability of the robot system, as shown in Fig. 15, the robot is loaded with 60 kg and moves freely on a cylindrical steel structure with a curvature diameter of 600 mm. Under the loading condition, the robot crawls steadily in the process of advancing (Fig. 15(c)), turning left (Fig. 15(a)), and turning right (Fig. 15(d)). There is no slip or fall, which verifies the stability of the robot's reliable load.

6.2. Cylindrical structure adaptive testing

The maximum tractive force of the robot is measured under dry and moist working conditions. The experimental process is shown in Fig. 16, and the experimental data are shown in Table 6.

To further validate the effectiveness of the adaptive mechanism, As shown in Fig. 17, the robot moves freely on two cylindrical steel structures with diameters of 600 mm and 750 mm. In all four cases, the robot's four wheels are in contact with the pipe, and the magnetic adsorption component provides sufficient adhesion to prevent the robot from falling. At first, the robot goes straight for a distance, then turns left, and finally turns right. Fig. 17(b) shows robot movement on a cylindrical structure with a diameter of 750 mm. The robot goes straight for a distance at first and then turns right until the rear wheel axis is parallel to the axis of the cylindrical steel structure.

To further verify the passive adaptive structure's effectiveness and magnetic adsorption's reliability. As shown in Fig. 18, the robot is placed on the underwater T-type cylindrical steel structure(vertical diameter 1000mm, horizontal diameter 900mm) and the diameter of 1800mm cylindrical steel structure in the same way to move freely.

To test the adsorption reliability of the conical magnetic adsorption wheel of the robot, the high-pressure water cleaning test with a pressure of 50MPa and a flow rate of 22 L/min, as shown in Fig. 19(a) and the cavitation jet test with a pressure of 20MPa, as shown in Fig. 19(b) and a flow rate of 67 L/min were carried out on a cylindrical steel structure with a diameter of 600mm. As shown in Fig. 20, the cavitation jet with the same pressure and flow rate was cleaned underwater. During the whole process, the magnetic adsorption wheel of the robot and the cylindrical steel structure are adsorbed reliably without any slippage.

The experimental results show that the magnetic adsorption force of the magnetic adsorption component is sufficient to support the robot in maintaining different postures and movement flexibility on the vertical cylindrical steel structure. Due to the passive adaptive structure, the four wheels of the robot can always keep in contact with the adsorption surface.

6.3. Integrative tests

A field cleaning experiment was carried out on the offshore platform to test the robot's comprehensive performance. In these experiments, regardless of the robot's posture, even if the robot moves to the air-sea interface, the robot's movement is not affected by anything. It never slips or rolls, as shown in Fig. 21. At the same time, the pressure of the cleaning equipment is 50 MPa, the flow rate is 22L/min, and the

cleaning efficiency of the robot can be achieved at 197 m²/h. Through the successful operation of the robot in the actual scene, the rationality and reliability of the robot design are verified.

7. Conclusion and future work

In this paper, a new type of wall-climbing cleaning robot based on the principle of magnetic adsorption is designed. The robot can move freely on the wall of the variable curvature cylindrical steel structure of the offshore platform and carry out cleaning operations.

- (1) A conical wheeled magnetic adsorption wall-climbing cleaning robot based on a two-degree-of-freedom adaptive structure is proposed. The robot can passively adjust its posture according to the curvature of the cylindrical structure to achieve free movement on the surface of variable curvature cylindrical structures. The adaptive structure of the robot and the design of the conical magnetic adsorption wheelsets are introduced in detail.
- (2) According to the structural parameters of the offshore cylindrical steel structure, the critical adsorption failure modes of the robot are theoretically analyzed and calculated. It is determined that the magnetic adsorption force of a single conical magnetic adsorption wheelset is at least 867 N when the safety factor is 1.1.
- (3) To obtain the parameters that have the most significant influence on the magnetic adsorption force, the structural parameters such as the cone angle of the conical magnetic adsorption wheel, the diameter of the cylindrical structure, and the angle between the conical magnetic adsorption wheel and the adsorption surface were optimized and analyzed. The coupling relationship between the cone angle and the adsorption force was obtained. After considering the working environment, the optimum cone angle of the conical magnetic adsorption wheel was determined to be 9°.
- (4) The prototype experiments' results show that the robot can fully use its structural characteristics to achieve passive self-adaptation on cylindrical structures of different diameters and has a specific load capacity, which verifies the robot structure's rationality and the adsorption operation's reliability.

Further work needs to be done, including using fan-shaped permanent magnets based on the Halbach array instead of annular permanent magnets to reduce the weight of the adsorption wheel and the magnetic flux leakage. Using sonar, IMU, and visual data for positioning, realize local map construction method and automatic path planning algorithm; the robot can also be equipped with obstacle avoidance sonar to detect and clean the cylindrical steel structure more safely. We will also complete erosion experiments on water jets and cleaning experiments on Marine biological samples. We will also build a visual underwater jet experimental device to observe and record the process of cleaning experiments. By optimizing the nozzle structure parameters, the cleaning efficiency is improved.

CRediT authorship contribution statement

Gaosheng Luo: Writing – review & editing, Writing – original draft.
Chuankun Luo: Writing – review & editing, Writing – original draft, Conceptualization.
Shimin Gao: Writing – review & editing.
Jingxiang Xu: Writing – review & editing.
Xuteng Bao: Writing – review & editing.
Zhiqiang Ma: Writing – review & editing.
Zhe Jiang: Writing – review & editing, Writing – original draft.

Declaration of competing interest

The authors declare that they have no known competing financial interests or personal relationships that could have appeared to influence the work reported in this paper.

Acknowledgments

This work was supported by the Shanghai Municipal Industrial Collaborative-Innovation Science and Technology Project [XTCX-KJ-2023-2-15] and the foundation from the Department of Natural Resources of Guangdong Province, GDNRC[2024]52. The authors thank the Shanghai Engineering Research Center of Hadal Science and Technology for their technical expertise and generous financial support. The authors would like to express their gratitude for the support of the Fishery Engineering and Equipment Innovation Team of Shanghai High-level Local University and China National Offshore Oil Corporation (CNOOC). Thanks for your invaluable assistance and support.

Appendix A. Supplementary data

Supplementary data to this article can be found online at <https://doi.org/10.1016/j.oceaneng.2024.119676>.

References

- Albitar, H., Ananiev, A., Kalaykov, I., 2014. In-water surface cleaning robot: concept, locomotion, and stability. *Int. J. Mechatron. Autom.* 4, 104–115.
- Callow, M.E., Callow, J.E., 2002. Marine biofouling: a sticky problem. *Biologist (London, England)* 49 (1), 10–14.
- Chang, Y., 2015. Development of a Wall Climbing Inspection Robot with High Mobility on Complex-Shaped Walls.
- Espinoza, R.V., Oliveira, A.S., Arruda, L.V., Neves, F., 2015. Navigation's stabilization system of a magnetic adherence-based climbing robot. *J. Intell. Robot. Syst.* 78, 65–81.
- Eto, H., Asada, H.H., 2020. Development of a wheeled wall-climbing robot with a shape-adaptive magnetic adhesion mechanism. In: Proceedings of the IEEE International Conference on Robotics and Automation (ICRA), vol. 2020, pp. 9329–9335. Paris, France.
- Guang-Ming, X., Jian-Wei, G., Zheng-Fei, X.U., Ji-Lian, L.U., 2003. Overview of Research on Skid-Steer Wheeled Mobile Robot. *Machine Tool & Hydraulics*.
- Han, L., Wang, L., Zhou, J., Wang, Y., 2021. The development status of ship wall-climbing robot. In: Proceedings of the 4th International Conference on Electron Device and Mechanical Engineering (ICEDME), Guangzhou, China, 2021, pp. 231–237.
- Huang, H., Li, D., Xue, Z., Chen, X., Shuyu, L., Leng, J., Wei, Y., 2017. Design and performance analysis of a tracked wall-climbing robot for ship inspection in shipbuilding. *Ocean Eng.* 131, 224–230.
- Hachicha, S., Zaoui, C., Dallagi, H., Nejim, S., Maalej, A.Y., 2019. Innovative design of an underwater cleaning robot with a two arm manipulator for hull cleaning. *Ocean Eng.* 181, 303–313.
- Lu, M.H., Shao, H., Chang, J., Liu, X., 2013. The research of models for TKY tubular joint welds in ultrasonic phased array inspection. *Adv. Mater. Res.* 779–780, 26–33.
- Jimenez-Martinez, M., 2020. Fatigue of offshore structures: A review of statistical fatigue damage assessment for stochastic loadings. *Int. J. Fatig.* 132, 105327.
- La, H.M., Dinh, T.H., Pham, N.H., Ha, Q.P., Pham, A.Q., 2019. Automated robotic monitoring and inspection of steel structures and bridges. *Robotica* 37 (5), 947–967.
- Le, A.V., Kyaw, P.T., Veerajagadheswar, P., Muthugala, M.A., Elara, M.R., Kumar, M., Nhan, N.H., 2020. Reinforcement learning-based optimal complete water-blasting for autonomous ship hull corrosion cleaning system. *Ocean Eng.* 220, 108477.
- Nguyen, S.T., Pham, A.Q., Motley, C., La, H.M., 2020. A practical climbing robot for steel bridge inspection. In: Proceedings of the IEEE International Conference on Robotics and Automation (ICRA), vol. 2020, pp. 9322–9328. Paris, France.
- Leon-Rodriguez, H., Hussain, S., Sattar, T., 2012. A compact wall-climbing and surface adaptation robot for non-destructive testing. In: Proceedings of the 12th International Conference on Control, vol. 2012. Automation and Systems, Jeju, Korea (South), pp. 404–409.
- Li, J., Wang, X.S., 2016. Novel omnidirectional climbing robot with adjustable magnetic adsorption mechanism. In: Proceedings of the 3rd International Conference on Mechatronics and Machine Vision in Practice (M2VIP), vol. 2016, pp. 1–5. Nanjing, China.
- Nguyen, S.T., La, H.M., 2019. Development of a steel bridge climbing robot. In: Proceedings of the IEEE/RSJ International Conference on Intelligent Robots and Systems (IROS), vol. 2019, pp. 1912–1917. Macau, China.
- Nguyen, S.T., La, H.M., 2021. A climbing robot for steel bridge inspection. *J. Intell. Robot. Syst.* 102.
- Nguyen, S.T., La, K.T., La, H.M., 2023. Agile robotic inspection of steel structures: A bicycle-like approach with multisensor integration. *J. Field Robot.* 41, 396–419.
- Poggi, L., Gaggero, T., Gaiotti, M., Ravina, E., Rizzo, C.M., 2020. Robotic inspection of ships: inherent challenges and assessment of their effectiveness. *Ships Offsh. Struct.* 17, 742–756.
- Silva, M.F., Barbosa, R.S., Oliveira, A.L., 2013. Magnetic Wheeled Climbing Robot: Design and Implementation.
- Pham, A.Q., La, A.T., Chang, E., La, H.M., 2021. Flying-climbing mobile robot for steel bridge inspection. In: Proceedings of the IEEE International Symposium on Safety, Security, and Rescue Robotics (SSRR), New York City, NY, USA, 2021, pp. 230–235.
- Pham, A.Q., Motley, C., Nguyen, S.T., La, H.M., 2022. A robust and reliable climbing robot for steel structure inspection. In: Proceedings of the IEEE/SICE International Symposium on System Integration (SII), Narvik, Norway, 2022, pp. 336–343.
- Tavakoli, M., Marques, L., Almeida, A.T.D., 2012. OmniClimber: an omnidirectional light weight climbing robot with flexibility to adapt to non-flat surfaces. In: Proceedings of the IEEE/RSJ International Conference on Intelligent Robots and Systems, vol. 2012. Vilamoura-Algarve, Portugal, pp. 280–285.
- Wang, B., Ni, Z., Shen, Y., Zhang, S., Shen, Q., Niu, X.W., 2022. Design and analysis of a wheel-leg compound variable curvature ship hull cleaning robot. *Ocean Eng.* 266, 112755.
- Wei, SONG, 2018. Optimization design and experimental research on magnetic components for wall-climbing robot. *J. Zhejiang Univ. (Eng. Sci.)* 52 (10), 1837–1844.
- Yang, P., Sun, L., Zhang, M., 2024. Design and analysis of a passive adaptive wall-climbing robot on variable curvature ship facades. *Appl. Ocean Res.* 143, 103879.
- Yang, W., Xiaojun, Z., Minglu, Z., Lingyu, S., 2021. Design and analysis of split-flexible wall-climbing robot with adaptive variable curvature façade. *J. Mech. Eng.* 57 (3), 49–58, 2021.
- Zhang, Z., Huang, X., Liu, H., Zhong, D., Yuan, M., Qi, Y., Lu, G., Sun, L., 2021. Analysis on mechanics and magnetic adsorption of wheeled wall-climbing and obstacle-jumping robot. In: Proceedings of the China Automation Congress (CAC), vol. 2021, pp. 6306–6310. Beijing, China.